

Supporting Information for "Overturning the Mediterranean Thermohaline Circulation"

Robin Waldman¹, Nils Brüggemann², Anthony Bosse³, Michael Spall⁴, Samuel Somot¹ and Florence Sevault¹

¹Centre National de Recherches Météorologiques (CNRM), Météo-France-CNRS, UMR3589, Toulouse, France

²University of Hamburg, Hamburg, Germany and Delft University of Technology, Delft, The Netherlands

³Bjerknes Center for Climate Research and Geophysical Institute, University of Bergen, Bergen, Norway

⁴Woods Hole Oceanographic Institution, Woods Hole, Massachusetts, USA

Contents of this file

1. Text SI1 "NEMOMED12 hindcast simulation" and Figure SI1 and SI2
2. Text SI2 "From the vorticity budget to vertical transports"
3. Text SI3 "Validation of vertical transports diagnosed from vorticity" and Figure SI3
4. Text SI4 "Sensitivity to the seasonal cycle", Figure SI4 and SI5 and Table SI1
5. Text SI5 "Sensitivity to lateral boundary conditions" and Figure SI6
6. Text SI6 "Measuring the Northern Current transport"

SI1: NEMOMED12 hindcast simulation

We use the ocean general circulation model NEMO (version 3.6, *Madec* [2008]) in a regional configuration of the Mediterranean Sea called NEMOMED12. It has been extensively validated in terms of deep convection in the northwestern Mediterranean Sea by *Waldman et al.* [2017] and in the Mediterranean Sea by *Beuquier et al.* [2012]; *Hamon et al.* [2016] who used a similar configuration. It has a curvilinear horizontal grid of resolution $\delta x = 5.5 - 7.5\text{km}$ with 75 vertical levels of resolution between 1m at surface and 130m at the bottom. It resolves typically one to two Rossby radii in the Mediterranean Sea [*Beuquier et al.*, 2012], hence it is eddy-permitting. Its bathymetry is extracted from MERCATOR - LEGOS version 10 1/120° resolution database [*Beuquier et al.*, 2012].

In terms of physics, we use in the horizontal a bilaplacian momentum diffusion operator ($-1.25 \times 10^{10} \text{m}^4/\text{s}$) to limit model dissipation at mesoscale. For tracers, we use a Laplacian isoneutral diffusivity operator ($60 \text{m}^2/\text{s}$) to parametrize mixing by unresolved eddies. We use a partial free slip lateral boundary condition: tangent velocities at the first unresolved coastal grid point are reduced by 60% with respect to the first resolved velocities. This ensures more realistic exchanges at Gibraltar Strait. In the vertical, mixing is driven by the Turbulent Kinetic Energy scheme [*Gaspar et al.*, 1990], by the parametrizations of convection and bottom friction. For convection, we use the Enhanced Vertical Diffusion scheme which imposes a vertical mixing coefficient of $10 \text{m}^2/\text{s}$ on tracers and momentum when static instabilities occur, comparable to observational estimates [*Margirier et al.*, 2017]. At the bottom, a quadratic friction is applied on the last level [*Beuquier et al.*, 2012] which depends on the bottom mean kinetic energy and on a tidal turbulent kinetic energy climatology [*Lyard et al.*, 2006].

We initialize NEMOMED12 from *Rixen et al.* [2005] data within the Mediterranean Sea and from ORAS4 reanalysis in the near-Atlantic [*Balmaseda et al.*, 2013]. The model is run from January 1980 to 2013, and results are analyzed in the 1990–

Corresponding author: Robin Waldman, robin.waldman@meteo.fr

2012 period, after a 10-year spin-up. It is forced at the surface by the dynamical downscaling of ERA-Interim reanalysis using the regional climate model ALADIN-Climate (Radu *et al.* [2008]). This forcing called ALDERA [Hamon *et al.*, 2016] provides momentum, water and heat fluxes at 12km resolution every 3h. The heat flux is applied with a Newtonian sea surface temperature (SST) restoration of $-40W/m^2/K$ which parametrizes coupling at the first order [Barnier *et al.*, 1995, 2006]. The average net heat fluxes (Fig. SI1a) are negative, meaning that the Mediterranean Sea loses heat to the atmosphere. This is particularly true to the north of the basin, at the location of intense regional winds (Mistral, Tramontane, Bora, Etesian). West of Gibraltar strait, we apply a Newtonian temperature, salinity and sea level restoration toward ORAS4 reanalysis plus the monthly sea level anomaly from the ESA Climate Change Initiative [Adloff *et al.*, 2017]. Finally, the river runoff dataset is taken from Ludwig *et al.* [2009] for the main river mouths listed in RivDis [Vörösmarty *et al.*, 1996]. The inputs from remaining rivers are distributed as a coastal runoff in each coastal grid point. The Dardanelles Strait is considered as a river mouth whose runoff is deduced from Stanev and Peneva [2001]. All restoration and runoff terms are monthly mean timeseries. The resulting net surface water flux (Fig. SI1b) is positive, that is dominated by evaporation, almost everywhere. This is particularly true to the south of the basin where the SST is highest, and at the location of the main regional winds, where surface winds are strongest.

The vertically-integrated circulation can be quantified with the barotropic streamfunction (BSF, Fig. SI2), defined as:

$$\nabla_h \text{BSF} = -\mathbf{k} \times \mathbf{U}_h$$

with ∇_h the horizontal gradient operator, \mathbf{k} the vertical unit vector and \mathbf{U}_h the vertically-integrated horizontal transport. The Mediterranean Sea is characterized with a mostly cyclonic circulation, as indicated by negative values for the BSF. It supports the view of a mostly cyclonic boundary current flow along the borders. Exceptions are the relatively stable Southern Ionian anticyclonic gyre [Hamon *et al.*, 2016; Pinardi *et al.*, 2013], the anticyclonic Balearic circulation, probably overestimated by NEMOMED12 as noted by Hamon *et al.* [2016], and semi-stationary mesoscale anticyclones in the Alborán, Algerian and Levantine Seas.

SI2: From the vorticity budget to vertical transports

The key to diagnosing vertical velocities from the vorticity budget is the involvement of its vertical gradient (the horizontal convergence) in the planetary vortex stretching term, a leading order contribution to the vorticity balance. The vorticity budget is deduced from the online storage of the zonal and meridional momentum trends, namely NEMOMED12's Reynolds Averaged Navier-Stokes equations with specific turbulent closure schemes (see SI1). Then applying its *Curl*, isolating the planetary vortex stretching term and vertically integrating from surface yields the balancing of vertical velocities in the vorticity equation.

The NEMOMED12 prognostic momentum equations [Madec, 2008] are given by:

$$\begin{aligned} \frac{\partial \mathbf{U}_h}{\partial t} &= -[(\nabla \times \mathbf{u}) \times \mathbf{u} + \nabla(\mathbf{u}^2)]_h - f\mathbf{k} \times \mathbf{U}_h - \frac{1}{\rho_0} \nabla_h P + \Delta(\kappa_h \Delta \mathbf{U}_h) + \frac{\partial}{\partial z}(\kappa_z \frac{\partial \mathbf{U}_h}{\partial z}) + \mathbf{F}_B \\ &= \mathbf{A}_h + \mathbf{A}_z - f\mathbf{k} \times \mathbf{U}_h - \frac{1}{\rho_0} \nabla_h P + \mathbf{D}_h + \mathbf{D}_z + \mathbf{F}_B \end{aligned} \quad (4)$$

with \mathbf{A}_h and \mathbf{A}_z the vector form lateral and vertical advection, $-f\mathbf{k} \times \mathbf{U}_h$ the Coriolis acceleration, $-\frac{1}{\rho_0} \nabla_h P$ the pressure gradient force, \mathbf{D}_h and \mathbf{D}_z the Bilaplacian horizontal and the turbulent vertical momentum diffusions and \mathbf{F}_B the bottom friction. Note that surface friction is included as a surface boundary condition to the vertical turbulent diffusion. An Asselin temporal filter adds up to ensure the conver-

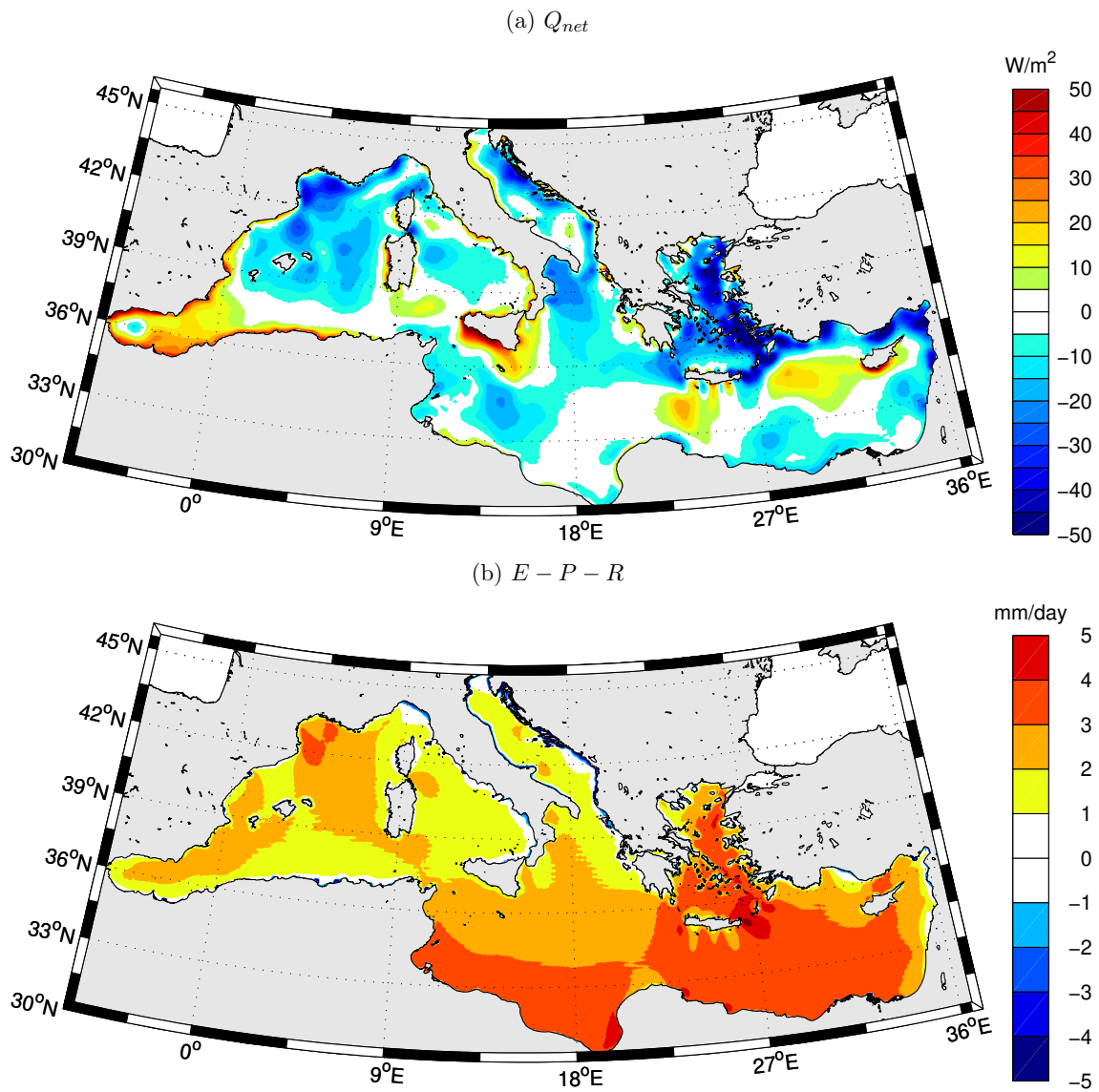


Figure SI 1. NEMOMED12 average net surface (a) heat (Q_{net} , W/m^2) and (b) water ($E - P - R$, mm/day) fluxes. Q_{net} includes turbulent and radiative flux forcings from ALDERA and the Newtonian SST restoration of $-40W/m^2/K$. $E - P - R$ includes the evaporation E and precipitation P from ALDERA and river / Dardanelles Strait runoffs R from Ludwig et al. [2009]; Vörösmarty et al. [1996]; Stanev and Peneva [2001].

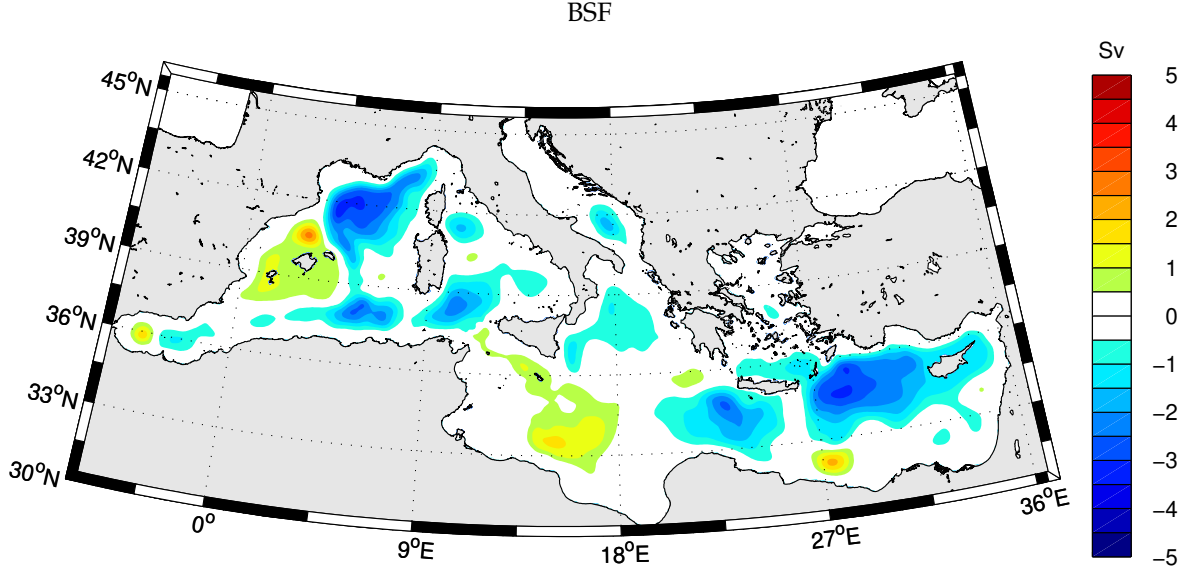


Figure SI 2. NEMOMED12 average barotropic streamfunction (BSF, Sv) quantifying the vertically-integrated volumic transport.

gence of even and odd timesteps in these prognostic equations, but we verified that it is several orders of magnitude lower than the dominant terms, so we neglect it in the following.

The vorticity equation is then deduced by applying the model's *Curl* operator $Curl(\mathbf{U}_h) = \frac{1}{\delta x \delta y} (\delta_{i+1/2}(v \delta y) - \delta_{j+1/2}(u \delta x))$ (with i and j the model's horizontal indices) to equation (4). This ensures that the *Curl* of all gradient terms vanishes in NEMOMED12's curvilinear grid, so that:

$$Curl\left(\frac{\partial \mathbf{U}_h}{\partial t}\right) = Curl(\mathbf{A}_h) + Curl(\mathbf{A}_z) - \beta v + f \frac{\partial w}{\partial z} + Curl(\mathbf{D}_h) + Curl(\mathbf{D}_z) + Curl(\mathbf{F}_B) \quad (5)$$

where the Coriolis term decomposes into the planetary beta effect $-\beta v$ and the planetary vortex stretching $f \frac{\partial w}{\partial z}$. We averaged this budget over the 1990–2012 period so that the momentum trend becomes several orders of magnitude lower than the leading-order terms and can reasonably be neglected. Hence, isolating the stretching term from equation (5), we get the following diagnostic vorticity balance (equation 1):

$$f \frac{\partial w}{\partial z} = \beta v - Curl(\mathbf{A}_h) - Curl(\mathbf{A}_z) - Curl(\mathbf{D}_h) - Curl(\mathbf{D}_z) - Curl(\mathbf{F}_B)$$

Finally, we integrate it vertically from surface to yield a vertical velocity from the vorticity balance. We assume no vertical velocity at surface, which induces small errors on the basin-integrated vertical transport (typically $10^{-3} Sv$ to $10^{-2} Sv$). We obtain equation 2:

$$w(z) = \frac{1}{f} \int_z^0 [-\beta v + Curl(\mathbf{A}_h) + Curl(\mathbf{A}_z) + Curl(\mathbf{D}_h) + Curl(\mathbf{D}_z) + Curl(\mathbf{F}_B)] dz$$

By integrating horizontally at specific depths and as a function of distance from the boundary, we obtain the contributions to vertical transports displayed in

Fig.1c-d and expressed for simplicity as equation 3:

$$Total = \beta + A_h + A_z + D_h + D_z + F_B + Res.$$

where *Res.* is the residual error. We evaluate comprehensively the method in the following SI3.

SI3: Validation of vertical transports diagnosed from vorticity

NEMO model's physical variables are expressed in Arakawa's C-grid, so that strictly speaking, the "stretching" vertical velocity w_{st} deduced from the vorticity equation is not equivalent to the actual velocity w . Indeed, the latter is located in the w-grid, to the center of each grid cell's upper face, whereas the former is located to the northeastern corner of it, above the f-grid where the vorticity budget is evaluated. Although this numerical consideration has little impact in the interior ocean, it is of paramount importance at the borders where highest w are located and thus also when integrating vertical transports over domains.

In order to make w and w_{st} comparable, it is necessary to interpolate w_{st} back to the w-grid and to smooth w in order to mimic all the ponderate average steps performed to retrieve w_{st} . We interpolate w_{st} to the w-grid by a 4-point average of each w_{st} value at the corners of the w face. In addition, both components of Coriolis have been interpolated from the u to the v-grid as u intervenes in the v equation and vice versa. Although the interpolation scheme used is the Energy and Enstrophy Conserving Scheme (EEN) and involves four triads, it can be reasonably approximated by a 4-point average of each u value at the corners of the v face, and reversely for v. Ultimately, w_{st} is comparable to a 9-point smoothing of the model w , so that:

$$\begin{aligned} w_{st}(i, j) = & \left[0.25w(i, j)V(i, j) + 0.125 \left(w(i-1, j)V(i-1, j) + w(i+1, j)V(i+1, j) \right. \right. \\ & \left. \left. + w(i, j-1)V(i, j-1) + w(i, j+1)V(i, j+1) \right) + 0.0625 \left(w(i-1, j-1)V(i-1, j-1) \right. \right. \\ & \left. \left. + w(i+1, j+1)V(i+1, j+1) + w(i+1, j-1)V(i+1, j-1) + w(i-1, j+1)V(i-1, j+1) \right) \right] / \\ & \left[0.25V(i, j) + 0.125 \left(V(i-1, j) + V(i+1, j) + V(i, j-1) + V(i, j+1) \right) \right. \\ & \left. + 0.0625 \left(V(i-1, j-1) + V(i+1, j+1) + V(i+1, j-1) + V(i-1, j+1) \right) \right] \end{aligned} \quad (6)$$

with i and j the horizontal indices and $V(i, j)$ the grid cell volume so that land points are masked. Hence we construct with equation (6) a smoothed vertical velocity w_{sm} from the model w and we compare vertical transports obtained from the three methods as well as from the sum of terms in equations 2 and 3. Note that in Fig.1c-d, the Total term is computed from the actual model w , whereas the *Res.* error term accounts for errors in equation 3 and errors in retrieving w_{sm} from w_{st} , but the smoothing step is not considered as error.

We investigate errors on vertical velocities and downwelling rate estimations as a function of depth in Fig. SI3. At LION location, within the DW area, the main difference between w_{st} and w is due to the inherent smoothing: indeed, there is large horizontal variability of w around this location (Fig.2a). However, the retrieval of w_{st} from the vortex stretching term and equation 2 compares very well to w_{sm} . When integrating transport horizontally within the open-sea DW region, the smoothing has almost no impact and errors are quasi-null, typically 1%. Now the integrated transport within domains that include boundaries such as the northwestern and eastern basins has relatively higher errors, typically of 10%. However, at the depths where each respective downwelling is evaluated, errors reach respectively 7% and

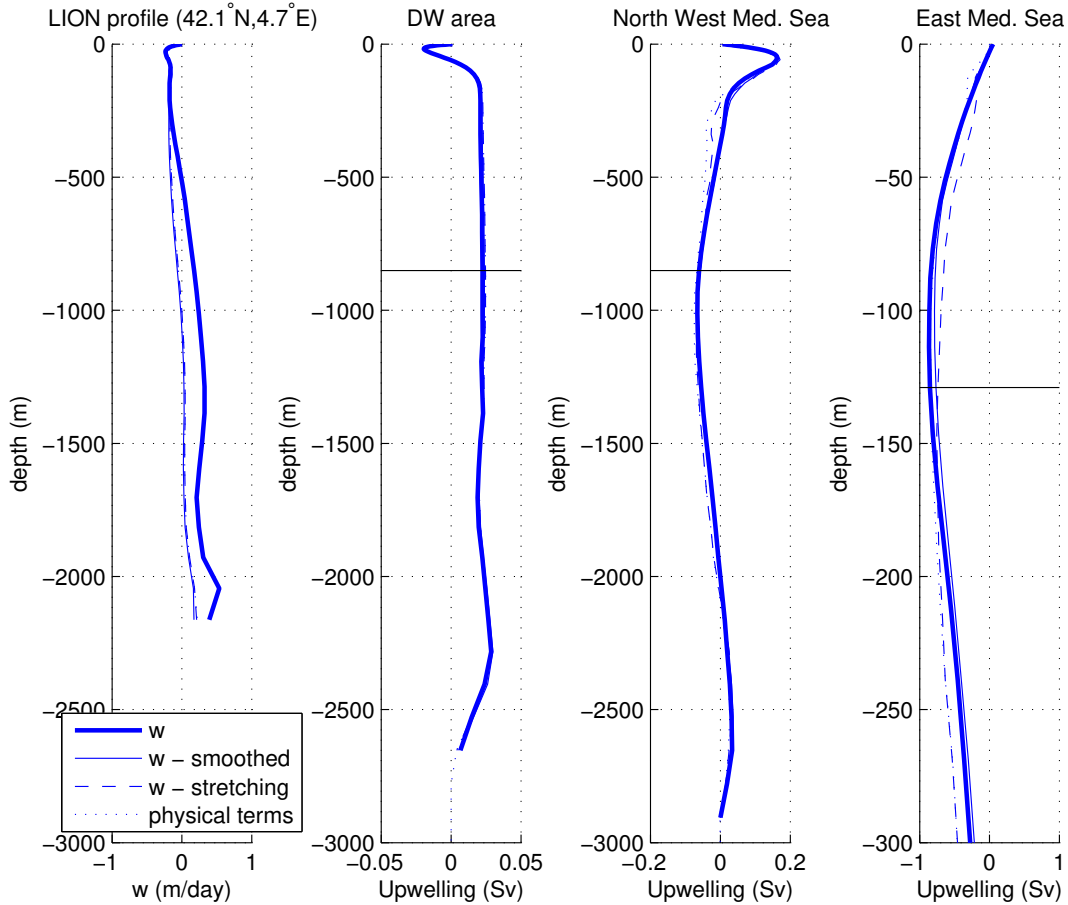


Figure SI 3. NEMOMED12 average vertical velocity (m/day) at LION profile ($42.1^{\circ}\text{N}, 4.7^{\circ}\text{E}$) and vertical transport in the DW area (see Fig.2a), the Northwestern and Eastern Mediterranean, as extracted from model velocity (w), from smoothed velocity (w_{sm}), from the stretching term of the vorticity equation (w_{st}) and from physical terms in the right hand side of equations 2 (for LION vertical velocity) and 3 (for vertical transports). The depth of each respective overturning is displayed by a black line when relevant.

3%. Hence, we take this as validation of the downwelling rate retrieval from the vorticity equation.

SI4: Sensitivity to the seasonal cycle

We proposed in this study a climatological mean view of the Mediterranean overturning circulation, but it might be variable over time, especially at the annual timescale if winter buoyancy losses drive it. In this respect, the deep western overturning displays a very intense annual cycle with maximum values in spring and early summer, whereas the eastern overturning has relatively weaker and more irregular seasonal variations (Fig. SI4). Although both cycles differ, we select the months of April (stronger than average) and October (weaker than average) to verify whether the main conclusions remain valid.

The coastal nature of downwelling remains unchanged throughout the year, with a sinking located within $\sim 50\text{km}$ of the boundary (Fig. SI5). Now some differences arise in individual basin contributions to the deep western and intermediate eastern downwelling (Table SI1). In April, the situation is similar to the annual mean

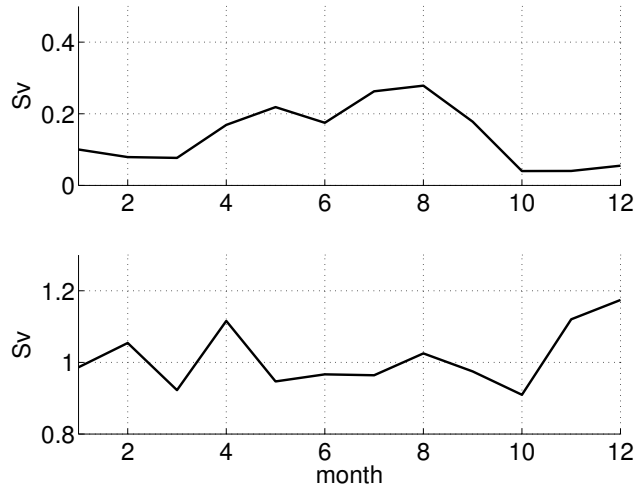


Figure SI 4. NEMOMED12 average seasonal cycle of the spatial maximum (top) western meridional overturning and (bottom) eastern zonal overturning.

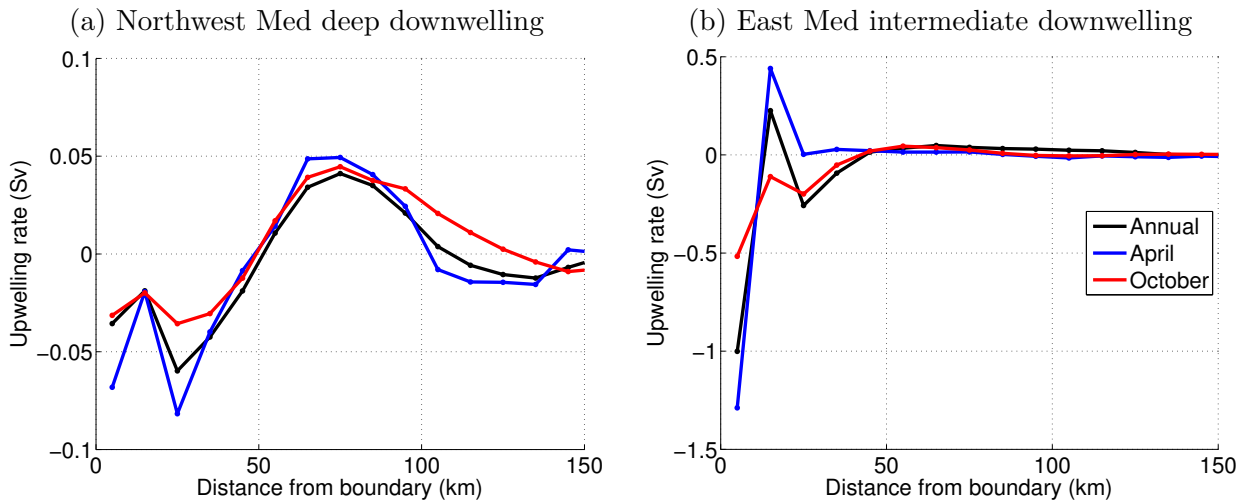


Figure SI 5. NEMOMED12 annual, April and October average (a) deep (930m depth) northwestern and (b) intermediate (129m depth) eastern upwelling rates as a function of distance from border.

for the deep downwelling with a domination of the northwestern Mediterranean Sea, and in particular the Northern Current, to the sinking. However, the Tyrrhenian Sea has a significant contribution to it, partly due to the deepening of sinking in both basins (not shown). To the east, the Adriatic Sea becomes important whereas the Ionian Sea has a negligible contribution to the intermediate downwelling. However, all boundary regions previously identified remain key downwelling areas. In October, the northwestern Mediterranean is no more a region of net deep downwelling, contrary to the Tyrrhenian Sea, but the Northern Current remains an area of significant downwelling. In the eastern Mediterranean, the intermediate downwelling is very similar to its annual mean with the same key boundary regions. In both basins and periods, all convection regions have a negligible contributions to the sinking.

Basin	Deep western upwelling rate	Basin	intermediate eastern upwelling rate
Western Mediterranean	0.00Sv / 0.00Sv	Eastern Mediterranean	-0.89Sv / -0.77Sv
Alborán	+0.12Sv / -0.03Sv	Adriatic	Total: -0.18Sv / -0.11Sv BC: -0.20Sv / -0.13Sv
Algerian	+0.02Sv / 0.00Sv	Aegean	Total: -0.37Sv / -0.15Sv CIW: -0.03Sv / +0.04Sv Archipelago (Total - CIW): -0.34Sv / -0.19Sv
Northwestern Mediterranean	Total: -0.09Sv / +0.05 DW: +0.03Sv / +0.06Sv BC-W: -0.02Sv / -0.06Sv BC-N: -0.10Sv / -0.04Sv BC-E: -0.09Sv / -0.02Sv	Ionian	Total: -0.05Sv / -0.28Sv BC-S: -0.15Sv / -0.22Sv BC-W: -0.05Sv / +0.01Sv BC-N: +0.21Sv / -0.10Sv
Tyrrhenian	-0.06Sv / -0.02Sv	Levantine	Total: -0.30Sv / -0.24Sv LIW: +0.02Sv / +0.12Sv BC-S: -0.15Sv / -0.23Sv BC-E: -0.05Sv / -0.05Sv BC-N: -0.05Sv / -0.01Sv

Table SI 1. Basin contributions to NEMOMED12 April / October average deep (930m) western and intermediate (129m) eastern sinking (Sv). Main downwelling regions are in bold.

We conclude that although both overturning cells display strong seasonal variations in their location and magnitude, the two main conclusions on the location of sinking remain valid throughout the year: convection areas are no net sources of downwelling, whereas the boundary current regions previously identified are. We have also diagnosed (not shown) that vertical transports can be accurately analysed from the vorticity balance for one month of the year, and the main physical balance remains unchanged.

SI5: Sensitivity to lateral boundary conditions

We have identified from the vorticity balance that the main source of equilibration for vortex stretching induced by downwelling is lateral dissipation near the boundary. It is likely dependent on the model numerics and in particular on lateral momentum boundary conditions. We address whether the boundary sinking and the vorticity balance found with partial free-slip boundary conditions still hold for full no-slip and free-slip conditions.

We diagnose the downwelling rate as a function of distance from the boundary in two twin simulations, differing only by the inclusion of full no-slip or free-slip lateral boundary conditions (Fig. SI6). In the former case, the first non-defined tangent velocities at the boundary are null, whereas in the latter, they are assumed equal to the last defined velocities at the boundary. Results show that for both downwelling cells, the sinking remains coastal in all cases, with however a $\sim 10\text{km}$ onshore shift of the deep western sinking with free-slip. Therefore, no matter the boundary condition, the stretching is successfully balanced in the vorticity equation near the boundary. Analysis of the vorticity balance reveals a similar picture as the control run under no-slip conditions, with lateral dissipation providing the net balance and lateral advection shifting the sinking offshore. Under free-slip, lateral dissipation remains the main balancing for the deep sinking, however bottom friction becomes important there and even the dominant term for the intermediate eastern sinking. We interpret this as follows: free-slip conditions intensify velocities down to the bathymetry, where bottom friction is hence enhanced and can provide the vorticity necessary to balance downwelling. Note that whereas lateral dissipation acts over $\sim 50\text{km}$, bottom friction is only applied to the lowermost model level and hence acts overwhelmingly at the first 10km from the boundary. We conclude that our results regarding the coastal location of downwelling are robust to lateral boundary conditions. We identify two main providers of balance in the vorticity equation, both being the result of interactions with topography: lateral dissipation and bottom friction.

SI6: Measuring the Northern Current transport

The Northern Current transport was estimated from repeated glider transects carried out in the framework of the MOOSE observatory [Testor *et al.*, 2017]. Here we focus on two sections off Nice and Perpignan, along the southern French coast, crossing the Northern Current (NC) at about 370km distance from each other. A total of $n_N = 113$ (Nice) and $n_P = 19$ (Perpignan) glider crossings of the NC were performed from 2007 to 2013. The glider underwater drift during each dive gives an estimate of the depth-average current and of the main flow orientation. Then the integration of the thermal wind balance from glider hydrographic sections yields the absolute geostrophic velocities normal to each NC crossing in a local streamwise coordinate system [Todd *et al.*, 2016].

Composites of potential density and cross-front velocities have been constructed by averaging individual sections in a normalized cross-stream axis. It was defined for each individual section with the origin set by the velocity maximum and the normalization factor set by the frontal width determined by fitting a Gaussian to the

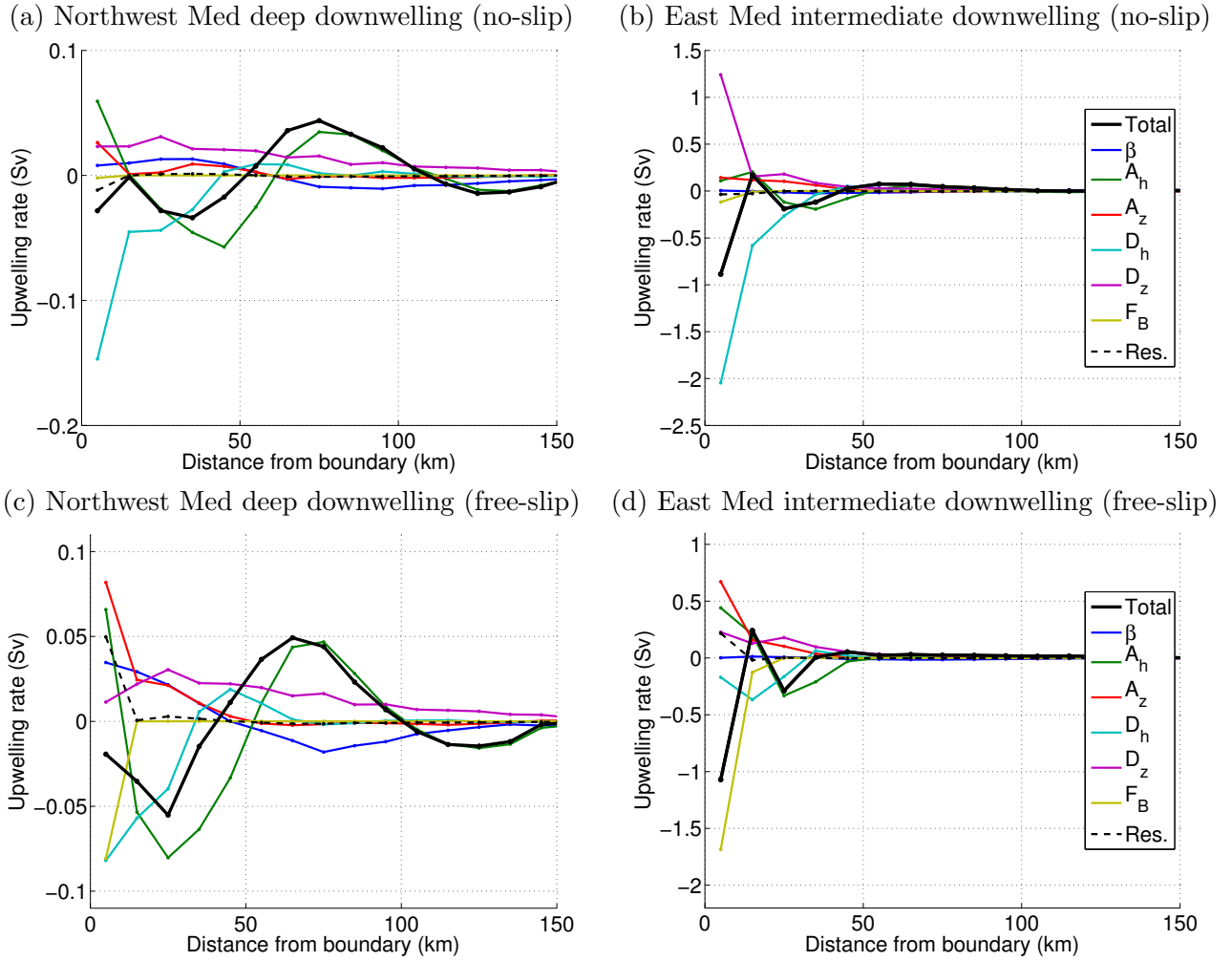


Figure SI 6. (a-b) No-slip NEMOMED12 average (a) deep (930m depth) northwestern and (b) intermediate (129m depth) eastern upwelling rates as a function of distance from border, as well as their vorticity balance (see equation 3). (c-d) Same as (a-b), under free-slip conditions.

upper 50m velocities [Bosse, 2015]. The step aims at removing spurious effects of the variable NC width on its average structure. For the two composites, the conversion back to physical units was done by considering the average current width. The origin corresponds to the NC peak velocities, with negative values toward the coast and positive values offshore (Fig.3b-c). The transport is then integrated from surface and from the coast to 45km off the velocity maximum, which corresponds to about three NC half-widths, and the downwelling (respectively upwelling) rate between both sections is deduced by continuity (Fig.3d) from the transport convergence (respectively divergence). Finally, observed velocity variances are estimated at each section (respectively V_N and V_P off Nice and Perpignan), then the error on average velocity differences ($\sqrt{V_N/n_N + V_P/n_P}$) is integrated spatially to deduce a confidence interval for the downwelling rate estimation (Fig. 3d, shaded).

References

- Adloff, F., G. Jordà, S. Somot, F. Sevault, T. Arsouze, B. Meyssignac, L. Li, and S. Planton (2017), Improving sea level simulation in mediterranean regional climate models, *Climate Dynamics*, doi:10.1007/s00382-017-3842-3.
- Balmaseda, M. A., K. Mogensen, and A. T. Weaver (2013), Evaluation of the ECMWF ocean reanalysis system ORAS4, *Quarterly Journal of the Royal Meteorological Society*, 139(674), 1132–1161.
- Barnier, B., L. Siefridt, and P. Marchesiello (1995), Thermal forcing for a global ocean circulation model using a three year climatology of ECMWF analyses, *J. Mar. Syst.*, 6(4), 363–380.
- Barnier, B., G. Madec, T. Penduff, J.-M. Molines, A.-M. Treguier, J. L. Sommer, A. Beckmann, A. Biastoch, C. Boning, J. Dengg, C. Derval, E. Durand, S. Gulev, E. Remy, C. Talandier, S. Theeten, M. Maltrud, J. McClean, and B. D. Cuevas (2006), Impact of partial steps and momentum advection schemes in a global ocean circulation model at eddy-permitting resolution, *Ocean Dynamics*, 56, 543–567.
- Beuvier, J., K. Béranger, C. L. Brossier, S. Somot, F. Sevault, Y. Drillet, R. Bourdallé-Badie, N. Ferry, and F. Lyard (2012), Spreading of the Western Mediterranean Deep Water after winter 2005: Time scales and deep cyclone transport, *J. Geophys. Res.*, 117, doi:10.1029/2011JC007679.
- Bosse, A. (2015), Circulation générale et couplage physique-biogéochimie à (sous-)mésoséchelle en méditerranée nord-occidentale à partir de données in situ, Ph.D. thesis, Université Pierre et Marie Curie.
- Gaspar, P., Y. Gregoris, and J. Lefèvre (1990), A simple eddy kinetic energy model for simulations of the oceanic vertical mixing: tests at station Papa and long-term upper ocean study site, *J. Geophys. Res.*, 95, 16,179–16,193.
- Hamon, M., J. Beuvier, S. Somot, J.-M. Lellouche, E. Greiner, G. Jordà, M.-N. Bouin, T. Arsouze, K. Béranger, F. Sevault, C. Dubois, M. Drevillon, and Y. Drillet (2016), Design and validation of MEDRYS, a Mediterranean Sea reanalysis over the period 1992-2013, *Ocean Science*, 12(2), 577–599, doi:10.5194/os-12-577-2016.
- Ludwig, W., E. Dumont, M. Meybeck, and S. Heussner (2009), River discharges of water and nutrients to the Mediterranean and Black Sea: major drivers for ecosystem changes during past and future decades?, *Progress in Oceanography*, 80(3), 199–217.
- Lyard, F., F. Lefevre, T. Letellier, and O. Francis (2006), Modelling the global ocean tides: modern insights from fes2004, *Ocean Dynamics*, 56(5), 394–415, doi: 10.1007/s10236-006-0086-x.
- Madec, G. (2008), NEMO ocean engine, note du Pôle de modélisation, Institut Pierre-Simon Laplace (IPSL), France, no 27 ISSN No 1288-1619.

- Margirier, F., A. Bosse, P. Testor, B. L'Hévéder, L. Mortier, and D. Smeed (2017), Characterization of convective plumes associated with oceanic deep convection in the northwestern mediterranean from high-resolution in situ data collected by gliders, *Journal of Geophysical Research: Oceans*, 122(12), 9814–9826, doi:10.1002/2016JC012633.
- Pinardi, N., M. Zavatarelli, M. Adani, G. Coppini, C. Fratianni, P. Oddo, S. Simoncelli, M. Tonani, V. Lyubartsev, S. Dobricic, and A. Bonaduce (2013), Mediterranean sea large-scale low-frequency ocean variability and water mass formation rates from 1987 to 2007: A retrospective analysis, *Prog. Oceanogr.*
- Radu, R., M. Déqué, and S. Somot (2008), Spectral nudging in a spectral regional climate model, *Tellus*, 60A, 898–910, doi:10.1111/j.1600-0870.2008.00341.x.
- Rixen, M., J.-M. Beckers, S. Levitus, J. Antonov, T. Boyer, C. Maillard, M. Fichaud, E. Balopoulos, S. Iona, H. Dooley, M.-J. Garcia, B. Manca, A. Giorgetti, N. Manzella, G. Mikhailov, N. Pinardi, and M. Zavatarelli (2005), The western Mediterranean deep water: A proxy for climate change, *Geophys. Res. Lett.*, 32(L12608), 1–4, doi:10.1029/2005GL022702.
- Stanev, E. V., and E. L. Peneva (2001), Regional sea level response to global climatic change: Black sea examples, *Global and Planetary Change*, 32(1), 33–47.
- Testor, P., L. Mortier, L. Coppola, H. Claustre, F. D'Ortenzio, F. Bourrin, X. Durrieu de Madron, and P. Raimbault (2017), Glider MOOSE sections, *Tech. rep.*, doi: <http://doi.org/10.17882/52027>.
- Todd, R. E., W. B. Owens, and D. L. Rudnick (2016), Potential vorticity structure in the north atlantic western boundary current from underwater glider observations, *Journal of Physical Oceanography*, 46(1), 327–348, doi:10.1175/JPO-D-15-0112.1.
- Vörösmarty, C., B. Fekete, and B. Tucker (1996), *Global river discharge database, RivDis*, UNESCO, Paris, international Hydrological Program, Global Hydrological Archive and Analysis Systems.
- Waldman, R., S. Somot, M. Herrmann, A. Bosse, G. Caniaux, C. Estournel, L. Houpert, L. Prieur, F. Sevault, and P. Testor (2017), Modeling the intense 2012–2013 dense water formation event in the northwestern Mediterranean Sea: Evaluation with an ensemble simulation approach, *Journal of Geophysical Research: Oceans*, 122(2), 1297–1324, doi:10.1002/2016JC012437.